

# COSMOGLOBE DR1. III. First full-sky model of polarized synchrotron emission from all WMAP and Planck LFI data

D. J. Watts<sup>1\*</sup>, U. Fuskeland<sup>1</sup>, R. Aurlien<sup>1</sup>, A. Basyrov<sup>1</sup>, L. A. Bianchi<sup>2</sup>, M. Brilenkov<sup>1</sup>, H. K. Eriksen<sup>1</sup>, K. S. F. Fornasier<sup>3</sup>, M. Galloway<sup>1</sup>, E. Gjerløw<sup>1</sup>, B. Hensley<sup>4</sup>, L. T. Hergt<sup>5</sup>, D. Herman<sup>1</sup>, H. Ihle<sup>1</sup>, K. Lee<sup>1</sup>, J. G. S. Lunde<sup>1</sup>, S. K. Nerval<sup>6,7</sup>, M. San<sup>1</sup>, N. O. Stutzer<sup>1</sup>, H. Thommesen<sup>1</sup>, and I. K. Wehus<sup>1</sup>

<sup>1</sup> Institute of Theoretical Astrophysics, University of Oslo, Blindern, Oslo, Norway

<sup>2</sup> Dipartimento di Fisica, Università degli Studi di Milano, Via Celoria, 16, Milano, Italy

<sup>3</sup> Instituto de Física, Universidade de São Paulo - C.P. 66318, CEP: 05315-970, São Paulo, Brazil

<sup>4</sup> Jet Propulsion Laboratory, California Institute of Technology, 4800 Oak Grove Drive, Pasadena, California, U.S.A.

<sup>5</sup> Department of Physics and Astronomy, University of British Columbia, 6224 Agricultural Road, Vancouver BC, V6T1Z1, Canada

<sup>6</sup> David A. Dunlap Department of Astronomy & Astrophysics, University of Toronto, 50 St. George Street, Toronto, ON M5S 3H4, Canada

<sup>7</sup> Dunlap Institute for Astronomy & Astrophysics, University of Toronto, 50 St. George Street, Toronto, ON M5S 3H4, Canada

October 20, 2023

## ABSTRACT

We present the first model of full-sky polarized synchrotron emission that is derived from all *WMAP* and *Planck* LFI frequency maps. The basis of this analysis is the set of end-to-end reprocessed COSMOGLOBE Data Release 1 sky maps presented in a companion paper, which have significantly lower instrumental systematics than the legacy products from each experiment. We find that the resulting polarized synchrotron amplitude map has an average noise rms of  $3.2 \mu\text{K}$  at 30 GHz and  $2^\circ$  FWHM, which is 30 % lower than the recently released BEYONDPLANCK model that included only LFI+*WMAP* *Ka*-*V* data, and 29 % lower than the *WMAP* *K*-band map alone. The mean *EE/BB* power spectrum ratio is  $0.40 \pm 0.02$ , with amplitudes consistent with those measured previously by *Planck* and QUIJOTE. Assuming a power law model for the synchrotron spectral energy distribution, and using the *T-T* plot method, we find a full-sky inverse noise-variance weighted mean of  $\beta_s = -3.07 \pm 0.07$  between COSMOGLOBE DR1 *K*-band and 30 GHz, in good agreement with previous estimates. In summary, the novel COSMOGLOBE DR1 synchrotron model is both more sensitive and systematically cleaner than similar previous models, and it has a more complete error description that is defined by a set of Monte Carlo posterior samples. We believe that these products are preferable over previous *Planck* and *WMAP* products for all synchrotron-related scientific applications, including simulation, forecasting and component separation.

**Key words.** ISM: general – Cosmology: observations, polarization, cosmic microwave background, diffuse radiation – Galaxy: general

## 1. Introduction

Understanding the polarization of the cosmic microwave background (CMB) is a primary focus of observational cosmology in the coming decades. There has been phenomenal observational success over the past few decades, from the satellite-based *COBE* (Smoot et al. 1992; Mather et al. 1994; Hauser et al. 1998), *Wilkinson Microwave Anisotropy Probe* (*WMAP*) (Bennett et al. 2013), and *Planck* (Planck Collaboration I 2020) experiments, to the many sub-orbital experiments including BICEP (Ade et al. 2021), ACT (Madhavacheril et al. 2023), CLASS (Eimer et al. 2023), SPIDER (SPIDER Collaboration et al. 2022), among many others. Future experiments, including the *LiteBIRD* satellite (LiteBIRD Collaboration et al. 2023), Simons Observatory (Ade et al. 2019) and CMB-S4 (Abazajian et al. 2019), will create the most sensitive maps of the polarized sky yet, providing the most stringent constraints on primordial gravitational waves.

In the past decade, uncertainties on cosmological constraints have been limited not only by instrumental sensitivity, but by incomplete knowledge of the sky itself. Uncertainty in the sky model has been mitigated by designing experiments with broad

frequency coverage, such as *WMAP* (Bennett et al. 2013) and *Planck* (Planck Collaboration I 2020), or analyzing maps from different experiments jointly (e.g., Bennett et al. 1996, Bennett et al. 2013, Planck Collaboration X 2016, and BICEP2/Keck Array and Planck Collaborations 2015, among many others). A major impediment to joint analyses is the difficulty of combining data with different survey strategies and incompletely characterized systematics. In order to maximize scientific throughput, one must either design an experiment that can characterize every relevant observable on its own, or jointly analyze different datasets in the same joint framework. In practice, joint analysis is often performed by combining datasets at the likelihood levels while marginalizing over known systematics.

The BEYONDPLANCK project performed such a joint analysis by combining external data, specifically, the Haslam 408 MHz map (Haslam et al. 1982), *WMAP* *Ka*-*V* bands, *Planck* 353 GHz in polarization, and *Planck* 857 GHz in intensity, while analyzing the *Planck* 30, 44, and 70 GHz time-ordered data (TOD) (BeyondPlanck Collaboration 2023). The *Planck* LFI experiment showed that raw detector sensitivity was not enough to obtain high-fidelity sky maps; Planck Collaboration II (2020) found that the detector gain solution depended on the assumed polarization and intensity of the sky. To break this circular depen-

\* Corresponding author: D. Watts; [duncanwa@astro.uio.no](mailto:duncanwa@astro.uio.no)

dency, the BEYONDPLANCK framework solved for the intrinsic sky signal and instrumental parameters iteratively, providing an accurate model of the entire system with full error propagation. By leveraging the external *WMAP*, Haslam, and *Planck* HFI data, BEYONDPLANCK was able to create *Planck* LFI maps of cosmological quality at all frequency channels, while generating a robust model of the foreground sky.

The COSMOGLOBE project<sup>1</sup> has generalized the BEYONDPLANCK analysis by additionally processing *WMAP*  $K$ – $W$ -band TOD jointly with *Planck* LFI TOD. This framework, fully described in Watts et al. (2023b) and Watts et al. (2023a), not only improved the quality of the *WMAP* maps themselves, but provided the most robust full-sky model of low frequency polarized emission available to date. In particular, poorly-measured modes due to transmission imbalance (Jarosik et al. 2007) have been effectively marginalized over, in large part due to the use of a global sky model that was not used in the fiducial *WMAP* analyses. The removal of poorly measured modes alone will improve Galactic modelling for years to come, as the current state-of-the-art models use *WMAP*  $K$ -band (23 GHz) maps as polarized synchrotron templates for modeling of synchrotron without any mitigation of the poorly-measured modes (Delabrouille et al. 2013; Thorne et al. 2017; Zonca et al. 2021).

In order to make use of the synchrotron model, we require robust estimates of the spectral behavior. Fundamental properties of synchrotron emission, such as the spectral index as a function of frequency, spatial decorrelation, and even the functional form of the spectral energy distribution (SED), are yet to be fully characterized observationally. Modern attempts have been frustrated by the lack of high signal-to-noise data; de Belsunce et al. (2022), for example, find spectral indices ranging from  $-5$  to  $-1$ , discrepant with predictions from direct measurements of the cosmic ray energy spectrum of  $2$ – $3$  (Rybicki & Lightman 1985; Orlando & Strong 2013; Neronov et al. 2017), largely due to fitting too many parameters to data with too low signal-to-noise ratios. Such analyses can be greatly improved by combining complementary data sets.

While the combination of as many datasets as possible would help to constrain polarized synchrotron’s large-scale properties, long-standing discrepancies between existing datasets complicate this. As shown by, for example, Planck Collaboration X (2016) and Weiland et al. (2018), there are discrepancies in the polarization measurements of *WMAP* and *Planck*, partially due to known instrumental effects (Bennett et al. 2013; Planck Collaboration II 2020). BeyondPlanck Collaboration (2023) largely resolved these issues for LFI, while Watts et al. (2023b) removed the poorly measured modes in *WMAP*. In the first COSMOGLOBE data release, of which this paper is a part, Watts et al. (2023a) demonstrated that the polarized maps resulting from these two experiments are consistent at the noise level after recalibrating both experiments jointly. At the same time, the new maps must be validated by a variety of analysis methods. As noted in, for example, Weiland et al. (2022), simply using a different analysis pipeline can result in different estimates of the underlying frequency map. As such, we take care to appropriately marginalize over instrumental effects in our spectral analysis, and attempt to find the physical reason for the differences between different pipelines.

With these longstanding discrepancies addressed, the main goal of the current paper is to derive the highest signal-to-noise ratio model of polarized synchrotron emission from *Planck* and *WMAP* data published to date, including both amplitude and

spectral index parameters. This work is organized as follows. In Sect. 2, we provide a brief overview of the data products and the COSMOGLOBE data processing. Section 3 discusses the polarization amplitude of the COSMOGLOBE synchrotron model, its overall uncertainty, and the power spectrum properties compared to external products. Section 4 estimates the synchrotron spectral index using both the  $T$ – $T$  plot method and Gibbs sampling using Commander, followed by discussions and conclusions in Sect. 5.

## 2. Data products

The data products used in this paper are the *WMAP* and *Planck* LFI maps, with most of the statistical weight coming from 23–33 GHz, or the *WMAP*  $K$  and  $Ka$  bands and LFI’s 30 GHz band. These frequencies are low enough that we can treat them as synchrotron tracers and hence ignore thermal dust and CMB emission, but not so low that we need to take into account effects like Faraday rotation, such as in S-PASS data (Krachmalnicoff et al. 2018; Fuskeland et al. 2021). We describe the legacy data products and the data products from the COSMOGLOBE *WMAP* reanalysis in the following subsections.

### 2.1. WMAP and Planck legacy products

*WMAP* was a NASA-funded satellite mission that observed from August 2001 to August 2010, designed to characterize the microwave sky well enough to measure the primary CMB anisotropies across the full sky down to a resolution of  $13'$  FWHM. Using a differential scanning strategy inspired by COBE/DMR, *WMAP* produced maps of the sky at 23 ( $K$ ), 33 ( $Ka$ ), 41 ( $Q$ ), 61 ( $V$ ), and 94 GHz ( $W$ ) in both polarization and total intensity (Bennett et al. 2013), with angular resolutions of  $53'$  at 23 GHz to  $13'$  at 94 GHz. The maps are available on the LAMBDA website.<sup>2</sup>

The *Planck* Low Frequency Instrument (LFI) produced 30, 44, and 70 GHz maps in both intensity and polarization, while the High Frequency Instrument (HFI) produced 100, 143, 217, 353 GHz maps in polarization and intensity, and 545 and 857 GHz maps in intensity alone. The LFI data have lower white noise and higher angular resolutions (of  $30'$ ,  $20'$ , and  $13'$  FWHM for 30, 44, and 70 GHz) than *WMAP*. In contrast to *WMAP*, the LFI measurements used a single horn, and the *Planck* scanning strategy followed rings closely aligned with ecliptic meridians. The *Planck* legacy datasets, PR3 (Planck Collaboration I 2020) and PR4 (Planck Collaboration Int. LVII 2020), are both publicly available on the *Planck* Legacy Archive (PLA).<sup>3</sup>

### 2.2. COSMOGLOBE products

A main goal of COSMOGLOBE is to perform joint end-to-end analyses on multiple data sets, preferably beginning from raw TOD. An important advantage of such end-to-end processing is that it offers a robust path to breaking internal degeneracies within and between different data sets, in general reducing the magnitude of systematic effects. The analysis described by Beyond-Planck Collaboration (2023) and Watts et al. (2023a) were performed on raw TOD, producing cosmological parameters using the Bayesian Gibbs sampler, Commander3 (Galloway et al. 2023).

<sup>2</sup> [https://lambda.gsfc.nasa.gov/product/wmap/dr5/m\\_products.html](https://lambda.gsfc.nasa.gov/product/wmap/dr5/m_products.html)

<sup>3</sup> <https://pla.esac.esa.int/>

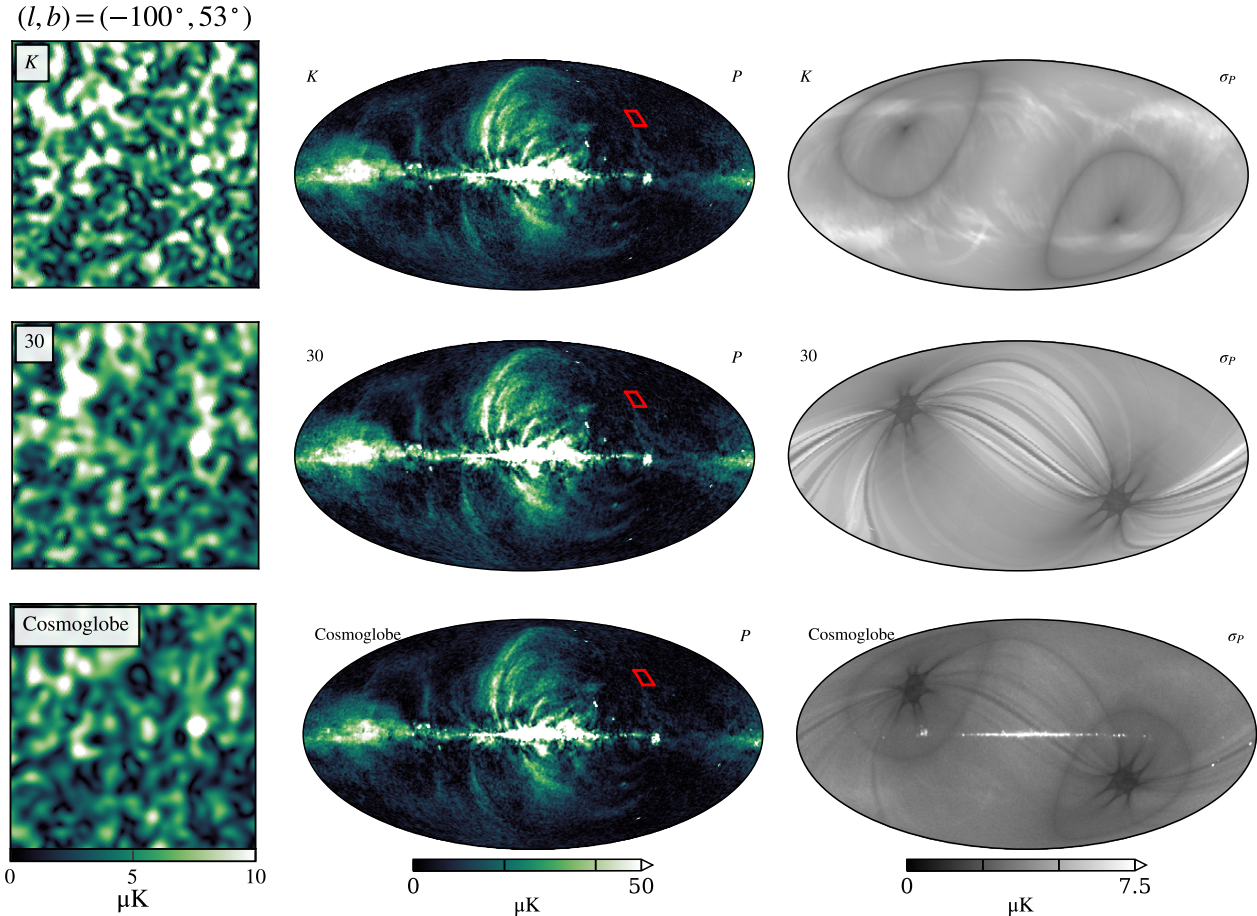


**Fig. 1.** Polarized intensity and white noise levels of (top): *WMAP* *K*-band, (middle): *Planck* 30 GHz, and (bottom): synchrotron amplitude from the COSMOGLOBE Gibbs chain, all evaluated at 30 GHz with a resolution of 72'. The leftmost column is a 10° width square centered a low signal-to-noise regions highlighted by a red square in the middle column's panels, the middle column shows the polarized total amplitude,  $P$ , and the rightmost column shows the rms noise for the frequency maps and the posterior standard deviation of the synchrotron amplitude.

In this framework, we produce a full sky model and set of instrumental parameters for each Gibbs sample, and the set of all such samples allows for a thorough characterization of the dependence of low-level instrumental parameters on the sky model. The sky model includes all relevant components in *WMAP* and LFI's frequency range, specifically the CMB, synchrotron, thermal dust, free-free emission, anomalous microwave emission, and radio point sources, the first three of which we model as polarized. The full products from this analysis and individual maps are available on the COSMOGLOBE website.<sup>4</sup>

As described by Watts et al. (2023a), COSMOGLOBE DR1 includes 500 end-to-end Gibbs samples, and we perform our basic analysis on each of these samples individually, then form posterior summary statistics from the full ensemble. This allows us to fully marginalize over the low-level systematic parameters, quantifying the extent to which instrumental processing propagates to the synchrotron spectral index determination.

### 3. Polarized synchrotron amplitude

In this section, we give an overview of the polarized synchrotron amplitude properties. In Sec. 3.1, we focus on the map-based properties, and compare with independently processed results in

Sec. 3.2. In Sec. 3.3, we evaluate the power spectrum of the polarized synchrotron map and compute the  $B$ -to- $E$  ratio.

#### 3.1. Polarization amplitude maps

We start by comparing the polarized spectral amplitude (as defined by  $P = \sqrt{Q^2 + U^2}$ ) from the COSMOGLOBE synchrotron map with the official *WMAP* *K*-band and *Planck* 30 GHz maps in the leftmost and middle columns of Fig. 1. The visible noise bias from plotting this nonnegative quantity highlights the reduction in the noise level in the COSMOGLOBE synchrotron map as compared to the *K*-band and 30 GHz maps. This is particularly visible in the leftmost column of Fig. 1, an inset of a high Galactic latitude, low signal region.

To quantify the noise improvement in the synchrotron maps over pure templates based on either *K*-band or 30 GHz maps, we compare the posterior standard deviation of the COSMOGLOBE synchrotron map with the frequency maps' rms values. The posterior standard deviation maps are  $\lesssim 1 \mu\text{K}$  for *K*-band, while temperature-to-polarization uncertainty in 30 GHz contributes at the  $2 \mu\text{K}$  level (see, e.g., Watts et al. 2023a and Basyyrov et al. 2023 for further details). An algorithmic smoothing prior of  $D_\ell = 200 e^{-\ell(\ell+1)\sigma^2} \mu\text{K}^2$ , where  $\sigma$  is the Gaussian width corresponding to a FWHM of 30', is applied during polarized synchrotron amplitude fitting, essentially downweighting low

<sup>4</sup> <https://www.cosmoglobe.uio.no/products/cosmoglobe-dr1.html>

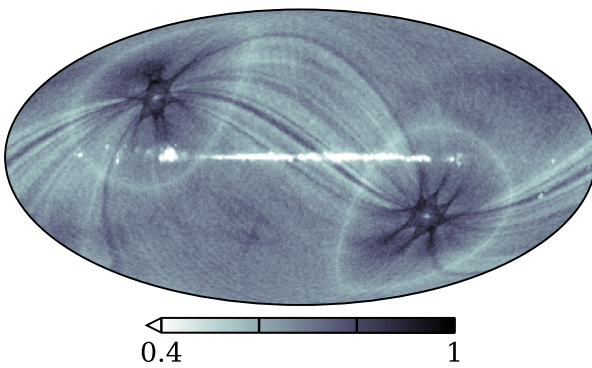


**Fig. 2.** Ratio between COSMOGLOBE and BEYONDPLANCK polarized synchrotron amplitude marginal posterior deviation per HEALPix  $N_{\text{side}} = 1024$  pixel.

signal-to-noise fluctuations at angular scales  $\lesssim 30'$ , or  $\ell \gtrsim 360$  (Svalheim et al. 2023a). Therefore, the rms noise contributions are relevant at roughly  $N_{\text{side}} = 128$ . To compare the COSMOGLOBE white noise level with the  $K$ -band and 30 GHz white noise levels, we simulate realizations of the expected white noise smoothed to  $72'$  and scale the maps to 30 GHz assuming  $\beta_s = -3.1$ , consistent with the post-processed synchrotron map. We display these smoothed rms maps in the right column of Fig. 1.

At these resolutions, the mean rms for  $K$ -band and 30 GHz are  $4.8 \mu\text{K}$  and  $4.7 \mu\text{K}$  respectively, compared to the mean value of  $3.4 \mu\text{K}$  for the COSMOGLOBE DR1 synchrotron map; this is consistent with adding the scaled maps in quadrature. While this may seem obvious on its face, the combination of *WMAP*  $K$ -band and *Planck* 30 GHz is not straightforward due to instrumental effects that remain in the maps, notably poorly measured modes in *WMAP* (Bennett et al. 2013; Weiland et al. 2018) and gain uncertainty in *Planck* (Planck Collaboration II 2020). These effects remain in the official *WMAP9* (Bennett et al. 2013) and *Planck* PR3/PR4 (Planck Collaboration II 2020; Planck Collaboration Int. LVII 2020) maps, making combination of these datasets non-ideal for Galactic science and cosmological analyses. However, the end-to-end BEYONDPLANCK (BeyondPlanck Collaboration 2023) products effectively removed the gain uncertainty modes from the *Planck* LFI maps, and the COSMOGLOBE DR1 results (Watts et al. 2023a) are free from the poorly measured modes. As shown in Fig. 46 of Watts et al. (2023a), the *Planck* 30 GHz and the *WMAP*  $K$ -band are consistent with each other at the  $10 \mu\text{K}$  level, which corresponds to white noise. This polarized synchrotron map, derived from consistent datasets, has a white noise level 29 % lower than both the  $K$ -band map and the 30 GHz map.

In Fig. 2 we plot the ratio between the COSMOGLOBE and BEYONDPLANCK (BeyondPlanck Collaboration 2023) synchrotron rms maps. Both these products are created using the Commander3 pipeline and similar data selection, but COSMOGLOBE benefits from additionally using the  $K$ -band data. The COSMOGLOBE synchrotron map has a mean posterior rms of  $3.4 \mu\text{K}$ , nearly a factor of two improvement over the BEYONDPLANCK map. As expected, the regions with the lowest ratios correspond to the deep *WMAP* observations and the Galactic plane, which benefit from the high signal-to-noise of the  $K$ -band data. Regions with nearly identical rms include regions with the highest *Planck* depth, such as the ecliptic poles, and regions less deeply observed by *WMAP*, corresponding to planet crossings and artifacts from the processing mask. Notably, stripes corre-

sponding the *Planck* scan strategy also show improvement with respect to BEYONDPLANCK. This is due to the interaction between the sky model and LFI's instrumental parameters – with the high signal-to-noise  $K$ -band data, the sky model becomes more stable, and LFI's relative gain solution becomes better determined.

### 3.2. Comparison with independent datasets

Next, we compare the COSMOGLOBE polarized synchrotron map with the frequency maps produced in the main DR1 chain, paying special attention to maps with the highest polarized synchrotron signal-to-noise ratio;  $K$ ,  $Ka$ , 30 GHz, and 44 GHz. Using the polarized synchrotron model generated in the main COSMOGLOBE DR1 chain, we evaluate the synchrotron emission at each frequency and subtract this from frequency maps produced by various different processing pipelines. We evaluate the COSMOGLOBE sky model using the `cosmoglobe` Python package using the full bandpass information of each instrument.<sup>5</sup>

The first and third rows of Fig. 3 show the *WMAP9* and PR3 residuals with respect to the COSMOGLOBE sky model in second and fourth rows. These residuals match previously-documented observational effects in both experiments. In particular, the *WMAP* maps show artifacts of the poorly-measured modes due to transmission imbalance in the differential horns (Jarosik et al. 2007; Bennett et al. 2013), while the PR3 differences are mostly due to relative gain errors (Planck Collaboration II 2020; Planck Collaboration Int. LVII 2020). In contrast, the synchrotron model matches the COSMOGLOBE DR1 frequency maps within  $5 \mu\text{K}$  across the sky, with few observational artifacts.

Most of the residuals are associated with the Galactic plane and diffuse structures uncorrelated with the *WMAP* and *Planck* observation strategies. The positive excess in the  $Ka$  Stokes  $Q$  map could be due to unmitigated data processing artifacts. While a similar large-scale excess can also be seen in the LFI 30 and 44 GHz Stokes  $Q$  maps, the signature strongly resembles the bandpass correction in *WMAP*  $K$ -band, suggesting incomplete treatment of bandpasses could be contributing to this large-scale signal. The LFI residuals, while much improved, still show trace residuals, especially near the Galactic center, that are somewhat correlated with the gain correction templates, but not at a level that high Galactic latitude features can be identified.

As the scale of instrumental residuals have been reduced to below the white noise level for each of the synchrotron-dominated full-sky polarization maps, we are now able to associate the residuals with potential modifications to the sky model. In Sec. 4, we analyze these maps allowing for spatial dependence in the polarized synchrotron spectral index to determine the extent to which true on-sky variation can be determined based on these maps.

### 3.3. Power spectra

Next, we consider the angular power spectrum of polarized synchrotron emission evaluated at 30 GHz. To estimate the power spectra without a noise bias, we perform a Commander3 run using half-mission splits with odd-numbered scans and even-numbered scans being analyzed in runs labeled HM1 and HM2. Each of these chains were performed using the same data as in the main COSMOGLOBE chain, with 200 samples each.<sup>6</sup> The high-

<sup>5</sup> <https://cosmoglobe.readthedocs.io/en/latest/tutorials/skymodel.html>

<sup>6</sup> These products can be found at [cosmoglobe.uio.no](http://cosmoglobe.uio.no).



**Fig. 3.** Frequency map minus sky model with respect to the CosmoGlobe DR1 sky model evaluated at 5°. CosmoGlobe maps are labeled CG, Planck 2018 maps are labeled PR3, and the legacy WMAP9 maps are labeled WMAP. Each of the WMAP9, Planck PR3, and CosmoGlobe maps have had the CosmoGlobe DR1 sky model evaluated at their respective bandpass and resolution subtracted.

est quality of similar half-mission splits that are publicly available are from the *Planck* PR3 analysis, as discussed in [Planck Collaboration IV \(2018\)](#). We therefore compute power spectra from the PR3 results and compare them directly with the CosmoGlobe HM splits.

We perform power spectrum estimation using NaMaster ([Alonso et al. 2019](#)) with the *Planck* 2018 common polarization mask with  $f_{\text{sky}} = 0.78$  and 1° apodization. To quantify the uncertainty, we take the cross spectrum for each pair of Gibbs samples from HM1 and HM2 respectively, and report the 68 % confidence intervals on this posterior. The power spectra are displayed in Fig. 4, and the standard deviation is computed using the within-bin variance of each bin, with the posterior standard deviation of the Gibbs chain added in quadrature for the CosmoGlobe spectra. Other than the very lowest and very highest multipole bins, there is good per-multipole agreement between both the PR3 and CosmoGlobe DR1 spectra. For comparison, we plot the *E*-mode power spectrum predicted by the *Planck* 2018 cosmological parameters.

Following [Planck Collaboration IV \(2018\)](#), we perform power law fits to the power spectra of the form  $\mathcal{D}_{\ell}^{\text{EE/BB}} = A_s^{\text{EE/BB}}(\ell/80)^{\alpha}$ , using multipoles  $\ell \in [2, 140]$ . The 68 % confidence intervals for each quantity, including the  $A_s^{\text{BB}}/A_s^{\text{EE}}$  ratio, are reported in Table 1. The primary differences between the fits to the two datasets are  $\sim 2\sigma$  discrepancies in the  $A_s^{\text{BB}}$  and  $\alpha_s^{\text{EE}}$  fits, while all others are consistent within  $\simeq 0.5\sigma$ . The primary drivers of these differences are lower  $\mathcal{D}_{\ell}^{\text{BB}}$  and higher  $\mathcal{D}_{\ell}^{\text{EE}}$  in the lowest bins.

A question of special interest is the ratio of synchrotron *B*-mode to *E*-mode power, which has been consistently noted to be less than one ([Page et al. 2007](#); [Planck Collaboration X 2016](#); [Planck Collaboration IV 2018](#); [Krachmalnicoff et al. 2018](#);

**Table 1.** Best-fit power law parameters to the synchrotron estimates evaluated at 30 GHz, using half-mission cross-spectra evaluated with NaMaster.

	PR3	CosmoGlobe
$A_s^{\text{EE}} [\mu\text{K}^2] \dots$	$2.39 \pm 0.07$	$2.35 \pm 0.05$
$A_s^{\text{BB}} [\mu\text{K}^2] \dots$	$1.09 \pm 0.06$	$0.94 \pm 0.04$
$A_s^{\text{BB}}/A_s^{\text{EE}} \dots$	$0.46 \pm 0.03$	$0.40 \pm 0.02$
$\alpha_s^{\text{EE}} \dots \dots$	$-0.81 \pm 0.02$	$-0.87 \pm 0.02$
$\alpha_s^{\text{BB}} \dots \dots$	$-0.80 \pm 0.03$	$-0.81 \pm 0.03$

[Rubiño-Martín et al. 2023](#); [Eimer et al. 2023](#)). The physical mechanism for this has been discussed in the context of Galactic magnetic fields and polarized thermal dust (e.g., [Kandé et al. 2017](#), [Hensley et al. 2022](#), [Vacher et al. 2023](#)), but similar mechanisms are likely to be in play for synchrotron polarization. In Table 1, we find a value of  $A_s^{\text{BB}}/A_s^{\text{EE}}$  of 0.40 for the CosmoGlobe splits and 0.46 for PR3. In this respect, we note that our value of  $A_s^{\text{BB}}/A_s^{\text{EE}}$  for *Planck* 2018 is higher than that reported by [Planck Collaboration IV \(2018\)](#) of 0.34, despite using nearly identical methodology. The origin of this discrepancy is not yet understood, but it must necessarily be associated with details in the power spectrum estimation algorithm.

#### 4. Polarized synchrotron spectral indices

Next, we turn our attention to the spectral energy density of polarized synchrotron emission, which we in this section will assume scales as a perfect power law in frequency,  $\nu^{\beta_s}$ . The determination of  $\beta_s$  across the sky has already been studied in detail using several different data combinations and methods. Al-

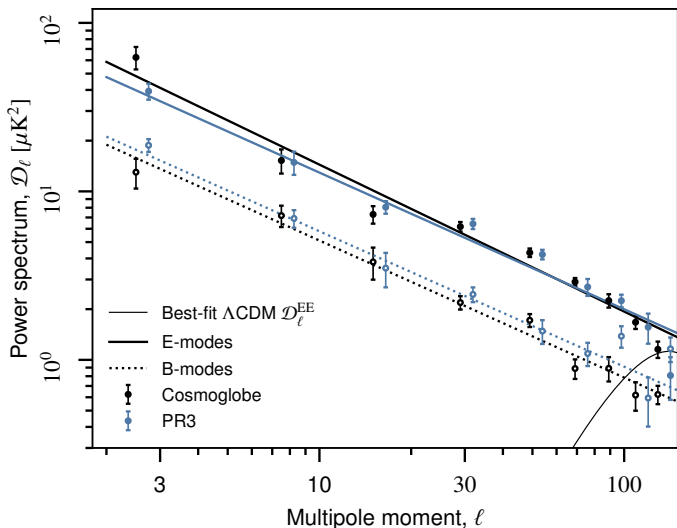


**Fig. 4.** Half-mission cross spectra for polarized synchrotron emission as evaluated for *Planck* PR3 (blue) and *Cosmoglobe* DR1 (black). Filled circles correspond to *E*-modes, while empty circles correspond to *B*-modes. The thick solid and dashed lines are the best-fit *E*- and *B*-mode power law fits to synchrotron, and the thin black line is the  $\Lambda$ CDM prediction for *E*-modes.

though the small-scale details vary, nearly every analysis has found  $\beta_s \simeq -2.8$  in the Galactic plane and  $\beta_s \simeq -3.3$  in high Galactic latitudes (Fuskeland et al. 2014; Krachmalnicoff et al. 2018; Fuskeland et al. 2021; Weiland et al. 2022), with the exception of QUIJOTE (Rubíño-Martín et al. 2023; de la Hoz et al. 2023), who find a slightly flatter spectral index along the Galactic plane. Both Fuskeland et al. (2014) and Weiland et al. (2022) report oscillations with Galactic longitude close to the Galactic plane, but high-latitude regions variations are more difficult to determine, and tend to depend on the specific dataset chosen and the analysis method chosen.

In order to probe the stability of our results with respect to algorithmic details, we perform two different analyses in the following, namely first a so-called *T-T* plot analysis in Sect. 4.1 and then a Gibbs sampling analysis using Commander1 in Sect. 4.2. Section 4.1 focuses on pairs of channels to better isolate potential unmodeled systematic effects, while Sect. 4.2 uses all *WMAP* and LFI channels plus *Planck* 353 GHz to maximize the joint statistical weight of all available data.

While the *Cosmoglobe* pipeline does produce samples of  $\beta_s$  as part of the main Gibbs chain, the full marginal signal-to-noise ratio per pixel with respect to  $\beta_s$  is generally very low due to degeneracies with respect to gain and bandpass uncertainties (Gjerløw et al. 2023; Svalheim et al. 2023b), and this makes it susceptible to systematic uncertainties. When sampled fully unconstrained,  $\beta_s$  often drifts to obviously non-physical values at high Galactic latitudes, essentially accounting for low-level gain and bandpass errors, and this in turns permits even the gain to drift into unphysical parameter regions. To avoid this, the default *Cosmoglobe* DR1 processing adopts an informative  $\beta_s \sim \mathcal{N}(-3.15, 0.05)$  prior sampling (Watts et al. 2023a). This choice has direct implications for the estimates of  $\beta_s$  presented in this section, which are derived from the *Cosmoglobe* frequency maps. To at least partially quantify this effect, we consider various different prior choices in Sect. 4.2, and we account for shifts resulting from different prior means into our final uncertainties.

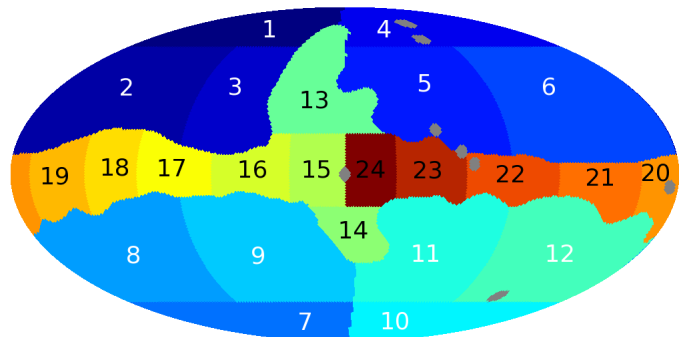


**Fig. 5.** Spectral index regions as defined in Fuskeland et al. (2014). The most prominent point sources are masked out and shown in grey circular areas.

#### 4.1. *T-T* plot analysis

The *T-T* plot analysis can be used for pairs of datasets in a model-independent way, allowing for us to probe the difference between different datasets without making strong assumptions on the underlying physical model. This method can also easily be adapted to probe the dependence on polarization angle. This can be used to determine both the orientation dependence of  $\beta_s$ , as well as identify the magnitude of unmodeled instrumental effects, such as beam asymmetries, as discussed in Wehus et al. (2013).

##### 4.1.1. Method

Following Fuskeland et al. (2014) and Fuskeland et al. (2021), we apply linear regression via the *T-T* plot method, in which spectral indices can be estimated over extended regions with approximately constant spectral indices. Here we use the regions labeled in Fig. 5. In this approach, our data model for two frequencies is

$$\mathbf{m}_\nu = \mathbf{m}_{\nu_0} \left( \frac{\nu}{\nu_0} \right)^{\beta_s} + c_\nu + \mathbf{n}_\nu, \quad (1)$$

where  $\mathbf{m}_\nu$  is a spatially varying amplitude map at frequency  $\nu$ ,  $\nu_0$  is the reference frequency,  $\beta_s$  the power law between the two frequencies,  $c_\nu$  the spatially constant offset per band, and  $\mathbf{n}_\nu$  the noise. In the case of noiseless data with no offset, the spectral index may be estimated using a simple ratio,

$$\frac{m_{\nu_1,p}}{m_{\nu_2,p}} = \left( \frac{\nu_1}{\nu_2} \right)^{\beta_{s,p}} \Rightarrow \beta_{s,p} = \frac{\ln(m_{\nu_1,p}/m_{\nu_2,p})}{\ln(\nu_1/\nu_2)}. \quad (2)$$

In the case where one map is much noisier than the other, the standard *T-T* plot method involves performing a linear regression  $\mathbf{m}_{\nu_1} = a\mathbf{m}_{\nu_2} + b$ , and associates  $\beta_s$  with  $\ln a / \ln(\nu_1/\nu_2)$ . More care must be taken when the noise amplitudes in both maps are comparable to each other, so we adopt the effective variance method of Orear (1982) as implemented by Fuskeland et al. (2014).

For the *T-T* plot analysis, we focus exclusively on bands between 23 and 33 GHz. As in Fuskeland et al. (2014), we use the *WMAP* *K* and *Ka* band Stokes *Q* and *U* parameter maps at 23 GHz and 33 GHz. The respective effective frequencies used are 22.45 GHz and 32.64 GHz. The maps originally at a HEALPix<sup>7</sup> pixelization of  $N_{\text{side}} = 512$  are downgraded to

<sup>7</sup> <http://healpix.sourceforge.net>



**Fig. 6.**  $T-T$  plots for Stokes  $Q$  and  $U$  maps of the COSMOGLOBE DR1  $K$ -band versus the COSMOGLOBE DR1 30 GHz (black) and the WMAP9  $K$ -band versus *Planck* PR3 30 GHz (red) for all regions. The horizontal (solid and dotted) lines indicate the corresponding inverse variance weighted values of the spectral index, averaged over rotation angle, and in the COSMOGLOBE case also weighted over samples.



**Fig. 7.** Synchrotron spectral index as a function of rotation angle, computed using  $T-T$  plot between the COSMOGLOBE DR1  $K$ -band and the COSMOGLOBE DR1 30 GHz (black) compared to the spectral index using the WMAP9  $K$ -band and *Planck* PR3 30 GHz (red) for all regions. The horizontal (solid and dotted) lines indicates the corresponding inverse variance weighted values of the spectral index, averaged over rotation angle, and in the COSMOGLOBE case also samples.

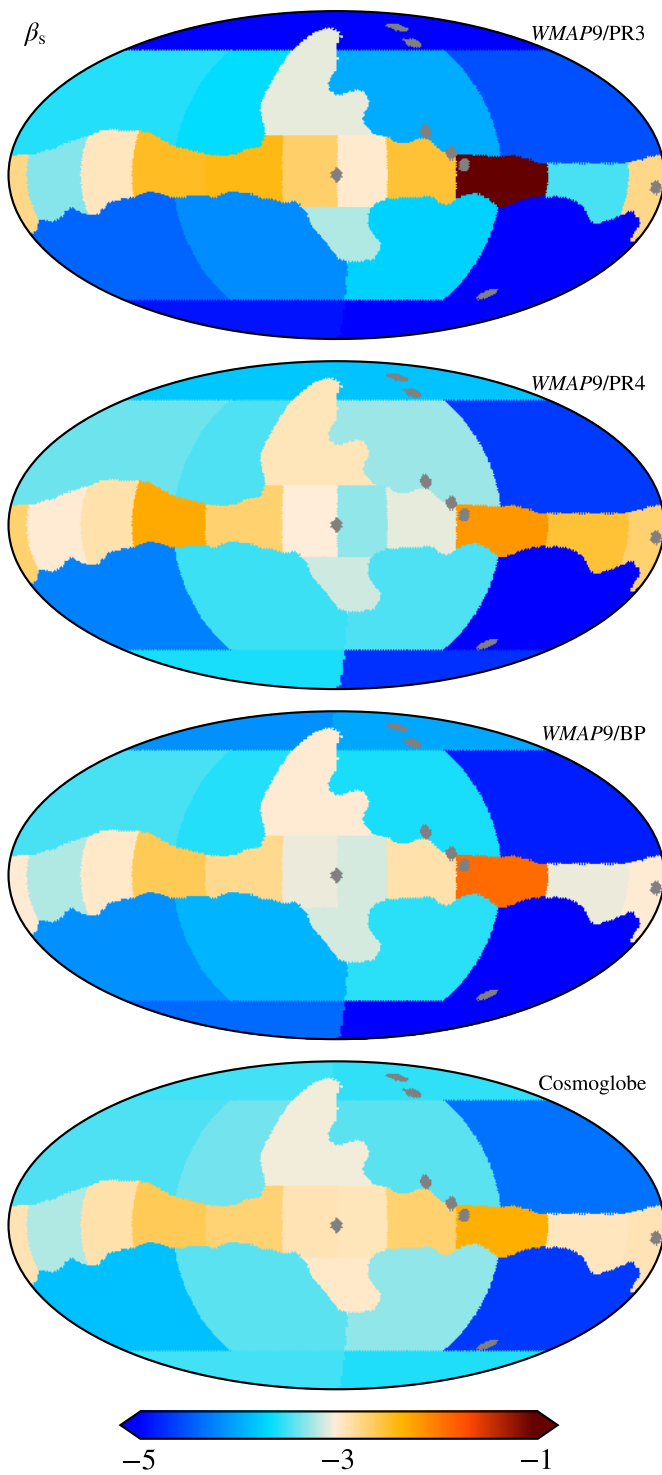


**Fig. 8.** Spatial variation of the synchrotron spectral index, computed using  $T-T$  plot between the (from top to bottom) *WMAP9 K-band and Planck PR3 30 GHz*, *WMAP9 K-band and Planck PR4 30 GHz*, *WMAP9 K-band and BEYONDPLANCK 30 GHz*, and *COSMOGLOBE K-band and COSMOGLOBE 30 GHz*. The spectral index is inverse variance weighted over rotation angle, and in the COSMOGLOBE case also samples.

$N_{\text{side}} = 64$  and smoothed to a common resolution of  $1^\circ$  FWHM. The *Planck* data products used are the 30 GHz Stokes  $Q$  and  $U$  maps, with an effective frequency of 28.4 GHz. Both the BEYONDPLANCK and COSMOGLOBE products are natively at  $N_{\text{side}} = 512$ , while for the *Planck* PR4, it is 1024.



**Fig. 9.** Synchrotron spectral index as a function of region number, computed using  $T-T$  plot between the *WMAP9 K-band and Planck PR3 30 GHz* (red), *WMAP9 K-band and Planck DR4 30 GHz* (blue), *WMAP9 K-band and BEYONDPLANCK 30 GHz* (purple), and *COSMOGLOBE K-band and COSMOGLOBE 30 GHz* (black). The spectral index is inverse variance weighted over rotation angles, and samples. The horizontal line in the high latitude regions corresponds to the estimated spectral index values from the *Planck* 2018 likelihood analysis (Planck Collaboration V 2020).

As in Fuskeland et al. (2021), a systematic uncertainty that takes into account the variation of  $\beta_s$  over rotation angle,  $[\max(\beta_{s,a}) - \min(\beta_{s,a})]/2$ , is added in quadrature to the statistical uncertainty. The uncertainty of the spectral indices is calculated as the minimum of the uncertainties in each rotation angle and region. For the COSMOGLOBE analyses we have a whole suite of maps represented by the individual samples instead of just one mean map. Here the standard deviation of the spectral indices of the samples is also added in quadrature to represent an additional systematic uncertainty. This enables us to have a better propagation of uncertainties from the maps to the final spectral indices.

#### 4.1.2. Results

We start by showing the full set of  $T-T$  scatter plots between *WMAP K-band* and *LFI 30 GHz* in Fig. 6. Red points show results for the official maps, while black points show the new COSMOGLOBE maps. Dashed black and solid red lines show best-fit linear fits, respectively. Overall, the two sets of point clouds appear to be in reasonable good agreement at this visual level. Perhaps the most notable features are the fact that while the best-fit lines are generally overlapping in most low Galactic latitude regions, the COSMOGLOBE slopes are generally a bit shallower than the official maps at high Galactic regions. The most discrepant case is region 22 along the Galactic plane, in which the best-fit line for the official maps are poorly aligned with the diffuse cloud, indicating that a substantial fraction of the pixels have anomalous values. This is typically indicative of strong systematic effects, for instance incomplete temperature-to-polarization leakage.

The information in Fig. 6 is significantly compressed in Fig. 7, which shows the best-fit spectral index as a function of polarization angle; for full discussion of this type of plots, see, e.g., Wehus et al. (2013) and Fuskeland et al. (2021). Variations in these curves could in principle be indicative of true spectral variations between the Stokes  $Q$  and  $U$  parameters, but very large variations are typically associated with uncorrected in-

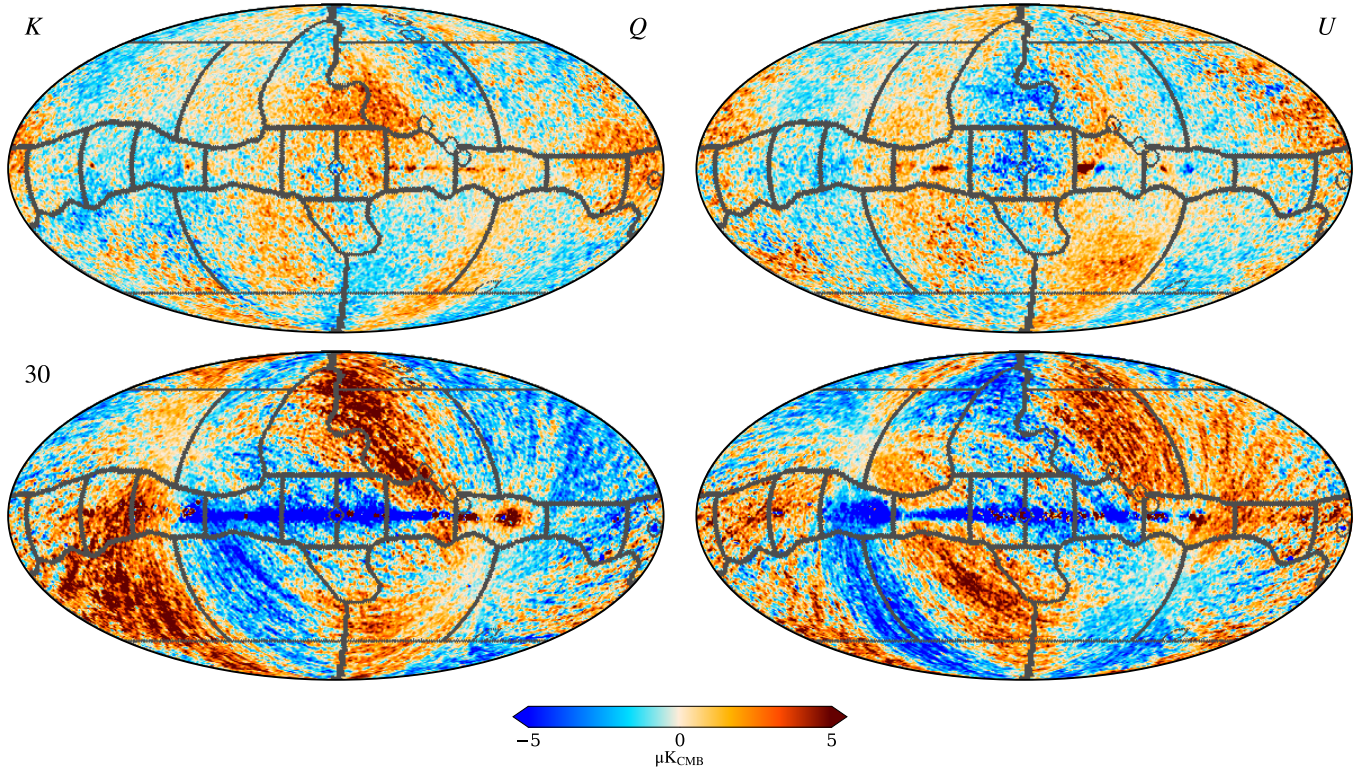


**Fig. 10.** Differences between the COSMOGLOBE and official WMAP 23 GHz (top row) and between COSMOGLOBE and *Planck* 2018 30 GHz (bottom row) maps with spectral index regions overlaid. Columns show Stokes  $Q$  and  $U$  parameters.



**Fig. 11.** Synchrotron spectral index computed using the  $T-T$  plot method with the COSMOGLOBE DR1  $K$ -band (23 GHz) and 30 GHz data versus COSMOGLOBE DR1  $K$ -band and  $Ka$ -band (33 GHz) data.

strumental systematic errors. Comparing the COSMOGLOBE (black curves) and official maps (red curves), we generally see that the former show less internal variations than the latter, suggesting greater consistency between the Stokes parameters. For region 22 we see that the official maps fall outside the plotted

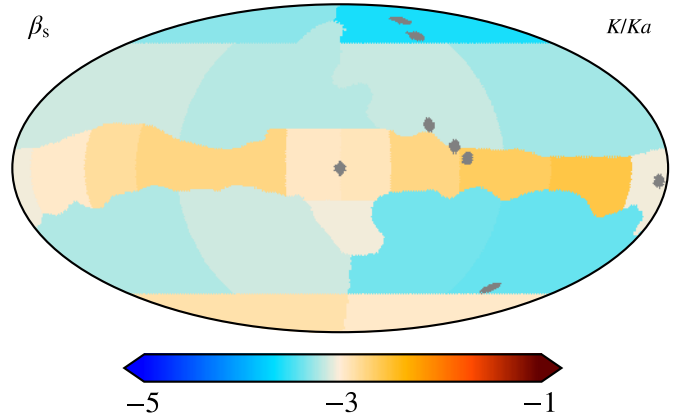


**Fig. 12.** Spatial variation of the synchrotron spectral index, computed using the  $T-T$  plot method between the COSMOGLOBE DR1  $K$ - and  $Ka$ -band. The spectral index is inverse variance weighted over rotation angle and samples.

range. As noted above, we inverse-variance weigh these results when reporting final co-added spectral indices in the following, and we include the Stokes' variation in the final uncertainties.

Figure 8 shows final spectral index estimates of this type for four different generations of *WMAP*  $K$ -band and *Planck* 30 GHz data in the form of regionalized sky maps. The top three maps show results derived from the official *WMAP*  $K$ -band map versus *Planck* PR3, PR4, and BEYONDPLANCK 30 GHz. The bottom map shows the results using the improved maps from the current COSMOGLOBE analysis. While all cases are inverse variance weighted over rotation angle, the COSMOGLOBE case is addition-



**Fig. 13.** Spectral index from COSMOGLOBE DR1 spectral index estimation,  $T-T$  plots with  $K/Ka$ , the QUIJOTE estimates, and the CLASS estimates.

ally averaged over posterior samples, accounting for low-level instrumental uncertainties. Some of the brightest point sources have been masked out using grey.

We see in this figure an overall narrowing in the range of spectral spectral indices, from regions with extreme values in the top map represented by dark red and blue values, with colors gradually fading in the lower figures. The range in the plot is quite wide for spectral indices, and goes from  $-5$  to  $-1$ . This improvement in the value of the spectral index is especially prominent in the high Galactic regions, as well as region number 22 along the Galactic plane. Using the COSMOGLOBE DR1 data, we find a full-sky inverse variance weighted mean of the spectral index of  $\beta_s = -3.07 \pm 0.07$ , while the mean of the high latitude regions 1–14 is  $\beta_s = -3.31 \pm 0.07$ .

The same results are also summarized in Fig. 9, with the spectral indices plotted as a function of region number. The different datasets are shown in different colors, and with the same order as the four maps in Fig. 8. Here we have also included one sigma uncertainties as errorbars as described in Sect. 4.1.1. The magnitudes of the error bars are set by the reported white noise level in each dataset except for COSMOGLOBE, which also takes into account systematic uncertainties through sample averaging. We also plot the estimated spectral index range for high Galactic regions, in our case represented by regions 1–12, as derived by the *Planck* 2018 LFI likelihood analysis (see Fig. 22 of [Planck Collaboration V 2020](#)). With each iteration of the data processing, the region estimates draw closer to this result.

When interpreting the variations between different data generations seen in Fig. 9, it is useful to overlay the region boundaries on the raw frequency map differences between the COSMOGLOBE and official *WMAP9* maps ([Watts et al. 2023a](#)); these are shown in Fig. 10 for the  $K$ -band and *Planck* 30 GHz maps. As discussed by [Watts et al. \(2023a\)](#), at high Galactic latitudes these large-scale patterns are largely dominated by different gain (for *Planck*) and transmission imbalance (for *WMAP*) estimates. The most extreme outlier in Fig. 9 is region 4, close to the North Galactic Pole, for which the official maps yield a mean spectral index of about  $\beta_s \approx -5$ . Inspecting Fig. 10, we see that that region has a strong eastward gradient from positive to negative in the *Planck* 2018 30 GHz difference, while the opposite is true for *WMAP*  $K$ -band. Similar considerations hold for many other regions as well.

Next, we consider similar  $T-T$  plots for the  $K$ -band and  $Ka$ -band maps. For the *WMAP* data, this analysis was already per-

formed in [Fuskeland et al. \(2014\)](#), so here we only present results using the new COSMOGLOBE data. First, as a consistency check, in Fig. 11 we plot the spectral indices for all 24 regions in the form of COSMOGLOBE  $K/30$  GHz versus COSMOGLOBE  $K/Ka$ . We see that for the regions in the north and south Galactic spurs, and along the Galactic plane (regions 13–24), there is a good agreement between the spectral indices obtained by the two pairs of datasets. Regions 1–12, all of which are high-latitude regions with low signal-to-noise, are consistent with the two data combinations. The most prominent outliers, regions 6 and 12, are the regions with the lowest signal-to-noise ratio, and hence most prone to unmodeled effects and noise fluctuations.

In Fig. 12 the value of the spectral indices is shown for the 24 regions. We see here that the colors are even fainter than the COSMOGLOBE  $K$ -band versus 30 GHz values (the bottom figure in Fig. 8), meaning there are fewer outliers with respect to a standard value in the range around  $-3$ . This is especially visible in the regions with lowest signal to noise, like regions 6, 8 and 12, at high latitude. Taking the inverse variance weighted mean of the spectral indices of all 24 regions, we get  $\beta_s = -2.95 \pm 0.07$ , while for the high latitude regions 1–14 we get  $-3.20 \pm 0.10$ .

#### 4.2. Parametric component estimation

In this section we use [Commander1](#)<sup>8</sup> to perform pixel-based component separation on maps smoothed to a common resolution of  $5^\circ$  and at  $N_{\text{side}} = 64$ .<sup>9</sup> For this analysis, we generate 100 pixel-based [Commander1](#) Gibbs samples for each of the 500 COSMOGLOBE DR1 Gibbs samples produced by [Commander3](#). This allows us to decompose the pure statistical error assuming white noise alone for each of the 100 [Commander1](#) samples, while changes between each main DR1 sample show the effects of low-level instrumental processing. In these analyses, we use the same polarized bands as in the main COSMOGLOBE DR1 analysis, namely *WMAP*, *Planck* LFI, and *Planck* 353 GHz. We use a prior  $\beta_s \sim \mathcal{N}(-3.1, 0.1)$  for the synchrotron spectral index, which is looser than the algorithmic prior used for the main DR1 processing. For thermal dust emission, we adopt the dust temperature map,  $T_d$ , from [Planck Collaboration X \(2016\)](#), coupled with a constant spectral index of  $\beta_d = 1.55$ ; minor variations in the thermal dust model has only a small impact on the synchrotron spectral index.

Overall, we consider the same data model as in COSMOGLOBE DR1, but now allow for a spatially varying  $\beta_s$  in two different forms. First, we allow  $\beta_s$  to vary over the same regions as in the  $T-T$  analysis. We find that for such large regions, there is only a small effect due to the prior. For instance, when considering very different priors of  $\mathcal{N}(-3.5, 0.1)$  and  $\mathcal{N}(-2.7, 0.1)$ , we find a maximum difference of  $\Delta\beta_s = 0.3$  in the lowest signal-to-noise region; generally it is much smaller than this. In the following, we add the resulting differences in quadrature to the uncertainty due to statistical and systematic errors to account for prior ignorance.

The results from this analysis are summarized in Fig. 13 for the nominal priors, and here we also compare our results with corresponding results derived by QUIJOTE ([de la Hoz et al. 2023](#)) and CLASS ([Eimer et al. 2023](#)). We choose these data sets because they are to date the most sensitive independent data

<sup>8</sup> <https://github.com/Cosmoglobe/Commander1>

<sup>9</sup> We use [Commander1](#) because it is parallelized over pixels and can quickly determine spatial variation for data with common angular resolution; [Commander3](#) is optimized for multi-resolution data, and therefore computationally much more expensive than [Commander1](#).

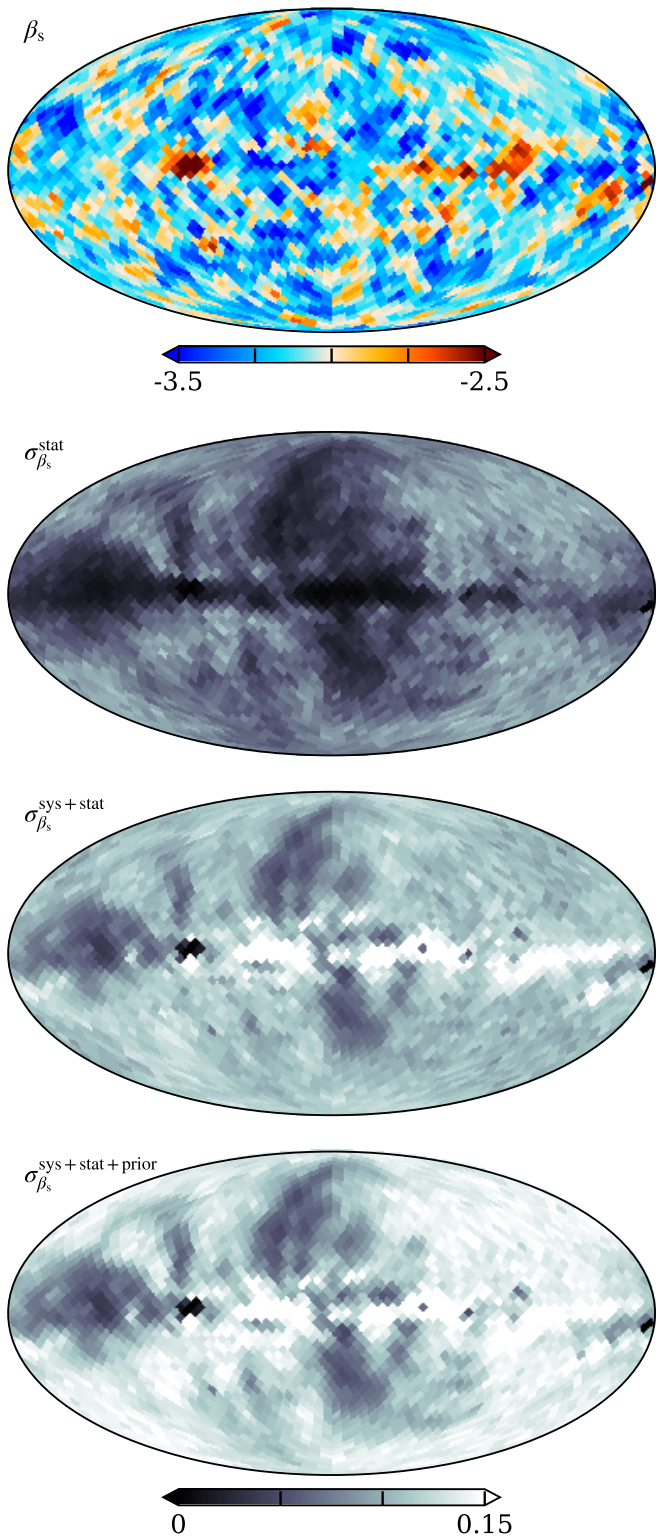


**Fig. 14.** COSMOGLOBE DR1  $\beta_s$  constraints. (First): Mean spectral index over all samples, (second): standard deviation over a single COSMOGLOBE DR1 sample, (third): standard deviation over all Commander1 and COSMOGLOBE DR1 samples, and (fourth): difference due to prior choice added in quadrature.

sets probing a frequency range that is comparable to *WMAP* and LFI; for comparison S-PASS is much more strongly affected by Faraday rotation (Krachmalnicoff et al. 2018; Fuskeland et al. 2021). The  $\beta_s$  maps delivered by the two projects are pixelized at  $N_{\text{side}} = 64$  and 32, respectively, with associated uncertainty maps taking into account the expected instrumental noise levels. We take an inverse-weighted average of the respective maps and report the weighted standard error within each region, displayed in Fig. 13.

In general, the uncertainties in our parametric analysis are smaller than each of the other published results, each for slightly different reasons. First, the  $T-T$  analyses will inherently have less constraining power than a full likelihood analysis, as this approach only uses two frequency channels via a linear regression, so the uncertainty is determined by the noise level in each frequency channel and the inherent variation within a given sky region. Beyond that, the  $T-T$  plot in this paper marginalizes over dependence on the polarization angle  $a$ , and by design accentuates systematic effects, such as beam ellipticity. Finally, the QUIJOTE analysis is most similar in data choice (MFI 11/13 GHz, *WMAP9 K/Ka*, *Planck PR4*) and methodology (B-SeCRET; de la Hoz et al. 2022), but still yields higher uncertainty than the Commander1 spectral index region analysis. This is most likely due to different spatial resolution and modeling choices; the Commander1 analysis presented here is performed at  $5^\circ$  resolution versus the  $2^\circ$  resolution per-pixel analysis in de la Hoz et al. (2023). In addition, de la Hoz et al. (2023) sampled for  $\beta_d$  and  $T_d$  with priors  $\mathcal{N}(1.55, 0.1)$  and  $\mathcal{N}(21, 3)$  while using a relatively wide prior on  $\beta_s$  of  $\mathcal{N}(-3.1, 0.3)$ .

At high Galactic latitudes (regions 1–12), there is good agreement between each of the treatments, and all values are consistent with a single constant value. In the north and south polar spur (regions 13 and 14) there is excellent agreement between all of the pipelines, while along the Galactic plane (regions 15–24), there are mild discrepancies between the methodologies, in particular a less distinct amount of periodic structure as a function of Galactic latitude.

To more finely probe the spatial variation of  $\beta_s$ , we perform a second Commander1 analysis with identical data and model choices, except  $\beta_s$  is now allowed to vary within each  $N_{\text{side}} = 16$  HEALPix pixel. We have found that this is the highest resolution grid in which the spectral index was not prior dominated across all high-latitude regions. In Fig. 14, we display the mean of all of the Gibbs samples, along with the standard deviation evaluated per COSMOGLOBE DR1 Gibbs sample,  $\sigma_{\beta_s}^{\text{stat}}$ , and the standard deviation over all COSMOGLOBE DR1 samples and Commander1 samples,  $\sigma_{\beta_s}^{\text{sys+stat}}$ . Thus,  $\sigma_{\beta_s}^{\text{stat}}$  is the standard deviation when the input maps themselves are static, and  $\sigma_{\beta_s}^{\text{sys+stat}}$  includes variations in the frequency maps themselves, corresponding to underlying instrumental effects, including gain, noise characterization, and baseline estimation. The uncertainty due to white noise alone traces the high signal-to-noise regions of the polarized synchrotron, especially the prominent loops and spurs and the Fan region. At high Galactic latitudes, the standard deviation is 0.1, indicating that the posterior uncertainty is limited by the prior. To further quantify this, we have performed additional Commander1 runs with priors of  $\mathcal{N}(-3.2, 0.1)$  and  $\mathcal{N}(-3.0, 0.1)$ , and adopt the deviation from the mean in the fiducial analysis as an estimate of the extent of prior domination,  $\sigma_{\beta_s}^{\text{prior}} \equiv (\langle \beta_{-3.0} \rangle - \langle \beta_{-3.2} \rangle)/2$ . Adding this in quadrature gives the total uncertainty, as shown in the bottom panel of Fig. 14.

The uncertainty across the entire Gibbs chain does not merely trace high signal-to-noise regions, and in fact there are



**Fig. 15.** Residual maps and normalized  $\chi^2$  in units of  $\sigma$  for the Commander1 analysis of the COSMOGLOBE DR1 data. Panels are organized with LFI channels in rows 1–2, WMAP in rows 3–7, and the total reduced  $\chi^2$  in row 8.

variations that exceed the prior surrounding the Galactic center. These variations are primarily due to gain and bandpass uncertainties. It therefore makes sense that gain variations in  $K$ ,  $Ka$ , and 30 GHz around the brightest region of the sky would induce large variations. Despite the relative increase in noise level when including instrumental effects, the brightest Galactic loops, the Cygnus region, and Tau A regions are well-constrained by the data.

As a final quality check, we display the residuals with respect to the Commander1 sky model in Fig. 15, as well as the total scaled and normalized  $\chi^2$ . In all bands but  $K$ , 30 GHz, and  $Ka$ , there are no visible artifacts due to instrumental uncertainty, with each map showing fluctuations consistent with the estimated white noise level calculated in the DR1 processing. In addition, many of the residuals visible in Fig. 3 have been reduced, demonstrating that polarized synchrotron spectral index variation provides meaningful improvements to the sky model fit.

The most salient remaining residuals are in  $K$ , 30 GHz, and  $Ka$ .  $K$ -band and 30 GHz are anticorrelated surrounding Galactic center, indicating tension between these two high signal-to-noise datasets. This could either be due to genuine mismodeling of the sky, or be due to incompletely modelled instrumental parameters. In particular, the signature is reminiscent of bandpass leakage corrections, which are shown, e.g., in Fig. 9 of Svalheim et al. (2023b).

A more persistent residual is found in the Stokes  $Q$   $Ka$ -band map. This feature has appeared in several different analyses, e.g., Fig. 4 of Svalheim et al. (2023a) and Fig. 8 of Weiland et al. (2022), but was not as clear without full removal of the poorly measured modes in the final map. The lack of this feature in the corresponding Stokes  $U$  map suggests that the effect is not a true Galactic effect, and is in some way due to instrumental processing, or unmodeled systematics; potential sources of this signal are discussed below.

## 5. Discussion and conclusion

We have presented a new state-of-the-art model of polarized synchrotron using the COSMOGLOBE DR1 data products, for the first time combining all *Planck* LFI and *WMAP* frequency maps and thereby leveraging the full statistical power of these data. The polarized synchrotron map as delivered in Watts et al. (2023a) has an effective white noise level of  $3.4\,\mu\text{K}$ , a 29 % improvement over the white noise levels of the *WMAP*  $K$ -band and LFI 30 GHz maps. This model characterizes the polarized sky signal to within  $5\,\mu\text{K}$  at all bands. We have also reproduced the previously-reported  $B$ -to- $E$ -mode ratio in the polarized synchrotron power spectrum. Furthermore, we have shown that physically reasonable spectral indices can be recovered using a variety of methods, which are consistent with both the methods presented in this paper and with previously published results from CLASS and QUIJOTE, confirming variation in  $\beta_s$  along the Galactic plane and constant at high Galactic latitudes.

Our improved processing of the *WMAP* and LFI data in conjunction with improved polarized synchrotron modeling has allowed us to dig deeper into the underlying differences between the two datasets. We have shown agreement between the  $\beta_s$  values derived using the  $T$ - $T$  plot using  $K/30\,\text{GHz}$  and  $K/Ka$  data combinations, further evidence that these datasets are now consistent with each other. The remaining unexplained differences between the sky maps and our derived model are primarily in the Galactic center, and have morphologies consistent with bandpass errors and SED complexities.

The least well-understood residual is in the  $Ka$ -band, specifically Stokes  $Q$ . Of all the known instrumental effects in both *WMAP* and *Planck* LFI, the only one that morphologically resembles this residual is the bandpass correction in  $K$ -band, which was previously presented in Fig. 12 of Watts et al. (2023a). The bandpass correction term depends solely on laboratory measurements, presented in Jarosik et al. (2003). The high statistical weight of  $K$ -band for determining polarized synchrotron could easily lead to an undersubtraction in the  $Ka$ -band maps. Conversely, the bandpass correction to  $Ka$ -band itself is negligible, as all of the  $Ka$ -band radiometers were reported to have nearly identical bandpasses. A full accounting of this effect, including sampling of bandpass differences in the *WMAP* TODs (not performed in Watts et al. 2023a) will be performed in future work.

The estimation of  $\beta_s$  is difficult precisely because the quantity is dependent on differences between different frequencies, which can often exacerbate systematic effects and processing choices. The differences between a sky model and datasets is best determined in the timestreams – much of the improvement demonstrated in this analysis would not have been possible through a purely map-based analysis. Beyond pure improvement of data quality, this approach allowed for a natural end-to-end propagation of errors, and demonstrated that some of the brightest regions of the sky in fact do not have well-determined spectral indices, despite their high signal-to-instrumental noise ratio. As increasingly stringent uncertainty constraints are becoming necessary in order to measure a non-zero tensor-to-scalar ratio, the use of joint information between experiments with complementary observation strategies will increasingly become a necessity. Future joint analyses, including for example QUIJOTE and CLASS data, will continue to improve our knowledge of the polarized sky.

*Acknowledgements.* We thank the entire *Planck* and *WMAP* teams for invaluable support and discussions, and for their dedicated efforts through several decades without which this work would not be possible. The current work has received funding from the European Union’s Horizon 2020 research and innovation programme under grant agreement numbers 819478 (ERC; COSMOGLOBE) and 772253 (ERC; brts2cosmology). In addition, the collaboration acknowledges support from RCN (Norway; grant no. 274990). This project has received funding from the European Union’s Horizon 2020 research and innovation programme under the Marie Skłodowska-Curie grant agreement No 101007633. The research was carried out in part at the Jet Propulsion Laboratory, California Institute of Technology, under a contract with the National Aeronautics and Space Administration (80NM0018D0004). We acknowledge the use of the Legacy Archive for Microwave Background Data Analysis (LAMBDA), part of the High Energy Astrophysics Science Archive Center (HEASARC). HEASARC/LAMBDA is a service of the Astrophysics Science Division at the NASA Goddard Space Flight Center. Some of the results in this paper have been derived using the `healpy` and `HEALPix`<sup>10</sup> packages (Górski et al. 2005; Zonca et al. 2019). This work made use of Astropy:<sup>11</sup> a community-developed core Python package and an ecosystem of tools and resources for astronomy (Astropy Collaboration et al. 2013, 2018, 2022).

## References

- Abazajian, K., Addison, G., Adshead, P., et al. 2019, arXiv e-prints, arXiv:1907.04473
- Ade, P., Aguirre, J., Ahmed, Z., et al. 2019, J. Cosmology Astropart. Phys., 2019, 056
- Ade, P. A. R., Ahmed, Z., Amiri, M., et al. 2021, Phys. Rev. Lett., 127, 151301
- Alonso, D., Sanchez, J., Slosar, A., & LSST Dark Energy Science Collaboration. 2019, MNRAS, 484, 4127
- Astropy Collaboration, Price-Whelan, A. M., Lim, P. L., et al. 2022, ApJ, 935, 167

<sup>10</sup> <http://healpix.sf.net>

<sup>11</sup> <http://www.astropy.org>

- Astropy Collaboration, Price-Whelan, A. M., Sipőcz, B. M., et al. 2018, AJ, 156, 123
- Astropy Collaboration, Robitaille, T. P., Tollerud, E. J., et al. 2013, A&A, 558, A33
- Basyrov, A., Suur-Uski, A.-S., Colombo, L. P. L., et al. 2023, A&A, 675, A10
- Bennett, C. L., Banday, A. J., Gorski, K. M., et al. 1996, ApJ, 464, L1
- Bennett, C. L., Larson, D., Weiland, J. L., et al. 2013, ApJS, 208, 20
- BeyondPlanck Collaboration. 2023, A&A, 675, A1
- BICEP2/Keck Array and Planck Collaborations. 2015, Phys. Rev. Lett., 114, 101301
- de Belsunce, R., Gratton, S., & Efstathiou, G. 2022, MNRAS, 517, 2855
- de la Hoz, E., Barreiro, R. B., Vielva, P., et al. 2023, MNRAS, 519, 3504
- de la Hoz, E., Diego-Palazuelos, P., Martínez-González, E., et al. 2022, J. Cosmology Astropart. Phys., 2022, 032
- Delabrouille, J., Betoule, M., Melin, J.-B., et al. 2013, A&A, 553, A96
- Eimer, J. R., Li, Y., Brewer, M. K., et al. 2023, arXiv e-prints, arXiv:2309.00675
- Fuskeland, U., Andersen, K. J., Aurlien, R., et al. 2021, A&A, 646, A69
- Fuskeland, U., Wehus, I. K., Eriksen, H. K., & Næss, S. K. 2014, ApJ, 790, 104
- Galloway, M., Andersen, K. J., Aurlien, R., et al. 2023, A&A, 675, A3
- Gjerløw, E., Ihle, H. T., Galeotta, S., et al. 2023, A&A, 675, A7
- Górski, K. M., Hivon, E., Banday, A. J., et al. 2005, ApJ, 622, 759
- Haslam, C. G. T., Salter, C. J., Stoffel, H., & Wilson, W. E. 1982, A&AS, 47, 1
- Hauser, M. G., Arendt, R. G., Kelsall, T., et al. 1998, ApJ, 508, 25
- Hensley, B. S., Clark, S. E., Fanfani, V., et al. 2022, ApJ, 929, 166
- Jarosik, N., Barnes, C., Greason, M. R., et al. 2007, ApJS, 170, 263
- Jarosik, N., Bennett, C. L., Halpern, M., et al. 2003, ApJS, 145, 413
- Kandel, D., Lazarian, A., & Pogosyan, D. 2017, MNRAS, 472, L10
- Krachmalnicoff, N., Carretti, E., Baccigalupi, C., et al. 2018, A&A, 618, A166
- LiteBIRD Collaboration, Ally, E., Arnold, K., et al. 2023, Progress of Theoretical and Experimental Physics, 2023, 042F01
- Madhavacheril, M. S., Qu, F. J., Sherwin, B. D., et al. 2023, arXiv e-prints, arXiv:2304.05203
- Mather, J. C., Cheng, E. S., Cottingham, D. A., et al. 1994, ApJ, 420, 439
- Neronov, A., Malyshev, D., & Semikoz, D. V. 2017, A&A, 606, A22
- Orear, J. 1982, American Journal of Physics, 50, 912
- Orlando, E. & Strong, A. 2013, MNRAS, 436, 2127
- Page, L., Hinshaw, G., Komatsu, E., et al. 2007, ApJS, 170, 335
- Planck Collaboration X. 2016, A&A, 594, A10
- Planck Collaboration I. 2020, A&A, 641, A1
- Planck Collaboration II. 2020, A&A, 641, A2
- Planck Collaboration IV. 2018, A&A, 641, A4
- Planck Collaboration V. 2020, A&A, 641, A5
- Planck Collaboration Int. LVII. 2020, A&A, 643, A42
- Rubiño-Martín, J. A., Guidi, F., Génova-Santos, R. T., et al. 2023, MNRAS, 519, 3383
- Rybicki, G. B. & Lightman, A. P. 1985, Radiative Processes in Astrophysics (New York, NY: Wiley)
- Smoot, G. F., Bennett, C. L., Kogut, A., et al. 1992, ApJ, 396, L1
- SPIDER Collaboration, Ade, P. A. R., Amiri, M., et al. 2022, ApJ, 927, 174
- Svalheim, T. L., Andersen, K. J., Aurlien, R., et al. 2023a, A&A, 675, A14
- Svalheim, T. L., Zonca, A., Andersen, K. J., et al. 2023b, A&A, 675, A9
- Thorne, B., Dunkley, J., Alonso, D., & Næss, S. 2017, MNRAS, 469, 2821
- Vacher, L., Aumont, J., Boulanger, F., et al. 2023, A&A, 672, A146
- Watts, D. J., Basyrov, A., Eskilt, J. R., et al. 2023a, arXiv e-prints, arXiv:2303.08095
- Watts, D. J., Galloway, M., Ihle, H. T., et al. 2023b, A&A, 675, A16
- Wehus, I. K., Fuskeland, U., & Eriksen, H. K. 2013, ApJ, 763, 138
- Weiland, J. L., Addison, G. E., Bennett, C. L., Halpern, M., & Hinshaw, G. 2022, ApJ, 936, 24
- Weiland, J. L., Osumi, K., Addison, G. E., et al. 2018, ApJ, 863, 161
- Zonca, A., Singer, L., Lenz, D., et al. 2019, Journal of Open Source Software, 4, 1298
- Zonca, A., Thorne, B., Krachmalnicoff, N., & Borrill, J. 2021, Journal of Open Source Software, 6, 3783